https://doi.org/10.5194/egusphere-2025-6331
Preprint. Discussion started: 4 January 2026

Operational performance of the Vaisala CL61 ceilometer for atmospheric profiling

Viet Le[1], Ewan J. O'Connor[1], Maria Filioglou[2], and Ville Vakkari[1, 3]

[1]Finnish Meteorological Institute, Helsinki, 00101, Finland
[2]Finnish Meteorological Institute, Atmospheric Research Centre of Eastern Finland, Kuopio, Finland
[3]Atmospheric Chemistry Research Group, Chemical Resource Beneficiation, North-West University, Potchefstroom, 2520, South Africa

Correspondence: Viet Le (viet.le@fmi.fi)

Abstract. The Vaisala CL61 is a new generation elastic backscatter lidar that extends conventional ceilometer capabilities by providing depolarization ratio measurements. Reliable use of these measurements, however, requires thorough evaluation and characterisation of the instrument performance and subsequent corrections applied. This study introduces a methodology for identifying the background signal and suitable liquid cloud layers for assessing the long-term behavior of multiple CL61 instruments deployed across various sites. Results indicate some variability between instruments, with most of these early production units exhibiting a pronounced decrease in laser power over time, accompanied by an increase in background noise. Normally, the instrument scales the internal calibration factor to compensate for changes in laser power and thus provide consistent attenuated backscatter coefficient values from profile to profile over time. However, for the instrument at the Lindenberg site, by performing manual calibration with atmospheric targets it was noted that once the laser power dropped below 40% there was no further compensation in the internal calibration factor.

The instrumental noise and bias, characterized using the termination hood, were found to vary with temperature. A method was developed for correcting for the instrumental bias and for estimating the associated uncertainty. Additionally, an aerosol inversion approach is presented for retrieving the profile of aerosol particle backscatter coefficient, aerosol depolarization ratio, and their corresponding uncertainties. In a case study, the aerosol-inverted and bias-corrected depolarization ratio was found to deviate by up to 0.1 from the original instrument-provided measurement. This demonstrates the importance of accounting for the molecular contribution when qualitatively interpreting aerosol measurements at the CL61 ceilometer operating wavelength of $905\,\mathrm{nm}$. Finally, signal loss in one unit was traced to optical lens fogging, and attributed to insufficient internal heating linked to the instrument's firmware behavior.

1 Introduction

Ceilometers are ground-based elastic backscatter lidars originally developed for the automated detection of cloud base height to support aviation and meteorological operations. Over the past two decades, advancements in both hardware and data processing have greatly enhanced their capabilities (Cimini et al., 2020). Notably, improvements in signal quality, particularly in signal-to-noise ratio, now enable ceilometers to provide profiles of attenuated backscatter coefficient with sufficient dynamic range to permit the observation of a wide range of atmospheric phenomena, including rainfall (e.g. Rocadenbosch et al., 2020; Roschke et al., 2025), fog (e.g. Haeffelin et al., 2016; Ribaud et al., 2021), icing (e.g. Hämäläinen et al., 2020), and even the quantitative estimation of aerosol concentrations (e.g. Shang et al., 2021; Filioglou et al., 2025). Ceilometer data are also increasingly used to estimate atmospheric boundary layer height (e.g. Kotthaus et al., 2023), which is a critical parameter for numerical weather prediction and air quality models (e.g. Uzan et al., 2020; Barragán et al., 2023). Their ability to operate autonomously and reliably in challenging environmental conditions makes them well-suited for long-term monitoring and integration into operational networks of national meteorological services and research institutions (e.g. Hirsikko et al., 2014). Many such organizations are actively investigating the use of ceilometer profile data to improve forecast model performance (e.g. Warren et al., 2018; Illingworth et al., 2019).

Vaisala has recently introduced the CL61 ceilometer with the capability of measuring the depolarization ratio, δ, which is the ratio of the perpendicular to the parallel component of the backscattered signal relative to the emitted polarization. This ratio provides insight into particle sphericity (e.g. Burton et al., 2012; Mamouri and Ansmann, 2016; Baars et al., 2017) and is essential for distinguishing various aerosol types (e.g. Illingworth et al., 2015; Nicolae et al., 2018; Floutsi et al., 2023; Filioglou et al., 2023; Le et al., 2024) such as pollen, smoke, dust, marine, and volcanic ash. It is also utilized in determining cloud phase (Sassen, 1991) and in the retrieval of cloud microphysical properties (Donovan et al., 2015).

To fully leverage the broad range of applications enabled by the CL61 ceilometer, including its new capability to measure the depolarization ratio, careful quality control of the backscattered signal from both polarizations is essential. Environmental conditions, such as temperature and relative humidity, can influence lidar performance (Campbell et al., 2002), making it necessary to assess their impact on data quality. For instance, Hervo et al. (2016) identified and corrected a temperature-dependent effect on the overlap function of a Lufft CHM15K ceilometer. Similarly, the older Vaisala CL31 ceilometer has been known to have backscatter artifacts below approximately $70\ \mathrm{m}$ (Van der Kamp, 2008; Martucci et al., 2010; Tsaknakis et al., 2011), prompting many studies to omit these near-surface measurements. Identifying and correcting such artifacts in the CL61 would enable reliable observations extending all the way to the surface. This capability is especially valuable for studying near-surface meteorological phenomena such as fog, haze, and emissions from ground-level aerosol sources.

In this study, we present a long-term evaluation of the CL61 ceilometer conducted at four different ACTRIS cloud profiling sites in Finland and Germany. Our analysis focuses on the impact of laser power on signal quality, the temperature sensitivity of the optical path, and methods for its correction. Additionally, we demonstrate our calculation of the uncertainty in the volume and particle depolarization ratio. Finally, we report instances of signal loss attributed to lens fogging observed in some of the CL61 units.

2 Instrument description

The CL61 ceilometer, manufactured by Vaisala, is a coaxial lidar system operating at a wavelength of $910.55\ \mathrm{nm}$ and equipped with depolarization measurement capability. Its key technical specifications are summarized in Table 1. In brief, the CL61 utilizes an InGaAs diode laser that emits linearly polarised pulses with an energy of $3.9\ \mu\mathrm{J}$ at a repetition rate of $9.5\ \mathrm{kHz}$.

Table 1. Specifications of the CL61 (CL61 User Guide: https://docs.vaisala.com/r/M212475EN-E/en-US, last access: 21 July 2025).

Specification	Values
Laser wavelength	910.55 nm
Laser	InGaAs diode
Beam divergence	± 0.2 mrad × ± 0.35 mrad
Measurement maximum range	15400 m
Reporting range resolution	4.8 m
Measurement interval	5 s
Pulse duration	160ns (at Full Width Half Maximum)
Pulse frequency	9.5 kHz
Maximum pulse energy	4.7μJ

Table 2. Firmware version of the CL61 across all the site locations

Site and coordinate	Time	Firmware version
Vehmasmäki	2022-01-01 to 2022-06-14	not stated
62.738°N, 27.543°E	2022-06-15 to 2023-04-27	1.1.10
	2023-04-28 to 2024-12-31	1.2.7
Hyytiälä	2022-01-01 to 2022-11-20	not stated
61.844°N, 24.287°E	2022-11-21 to 2023-11-22	1.1.10
	2023-11-23 to 2024-12-31	1.2.7
Kenttärova	2022-01-01 to 2022-06-20	not stated
67.987°N, 24.243°E	2022-06-21 to 2024-12-31	1.2.7
Lindenberg 52.208°N, 14.118°E	2024-03-01 to 2024-12-31	1.1.10

The instrument features a single-lens optical design and performs depolarization measurements using a single-receiver with an avalanche photodiode (APD) detector that switches between two polarising filters (one perpendicular and one parallel to the polarisation of the transmitted pulses) in the same coaxial optical path. Full overlap between the transmitted laser beam and the receiver field of view is achieved at approximately 250 m above ground level, with a maximum detection range of 15.4 km.

Data collected up to December 2024 from four CL61 ceilometers deployed at four different ACTRIS Cloudnet sites were analyzed. Three of these instruments are situated in Finland: Hyytiälä, Vehmasmäki, and Kenttärova, while the fourth is located in Lindenberg, Germany. The firmware versions of the instruments, along with their respective periods of validity, are presented in Table 2. The data from this study were obtained from the ACTRIS Cloudnet data portal (Görsdorf et al., 2025).

The CL61 is equipped with an internal heater to stabilize the temperatures of the laser and optical components. It includes a window heater and blower to maintain stable window conditions, as the window's transmission efficiency significantly affects the backscattered signal (see Sect. 4.3). The instrument's firmware continuously monitors and reports various housekeeping variables, such as internal temperature, laser temperature, window condition (calculated internally on a scale from 0% for a fully obstructed window to 100% for a clean window), and the status of the window blower heater. The quantity and type of variables reported may differ based on the firmware version.

The CL61 operates by emitting pulses of polarized laser light into the atmosphere and recording the backscattered signal. The received power per laser pulse is described by the lidar equation (Wandinger, 2005):

$$P(r) = \frac{1}{r^2} C_L O(r) \beta(r) e^{-2\int_0^r \alpha(r')dr'} + B. \tag{1}$$

Here, $O(r)$ is the overlap function that is unique to each instrument and is provided by the manufacturer. The coefficients α and β represent atmospheric extinction and backscatter, respectively, B is the background noise, and C_L represents the lidar constant. This constant encapsulates the system-specific characteristics of the lidar, such as its receiver optics and laser properties. It is initially determined and provided by the manufacturer, but it may drift over time as the instrument ages and its performance changes. Although the internal firmware attempts to monitor and compensate for these changes, additional calibration, such as absolute calibration using stratocumulus clouds (O'Connor et al., 2004; Hopkin et al., 2019), is still necessary.

The instrument provides two main output signals, $ppol$ and $xpol$ in arbitrary unit [a.u.], which represent the normalized and background-, range- and overlap-corrected parallel- and cross-polarized components of the attenuated backscattered signal (${}^{\parallel}\beta'$ and ${}^{\perp}\beta'$ respectively). They can be defined as

$$ppol = {}^{\parallel}\frac{(P(r)-B)r^2}{C_L O(r)} = {}^{\parallel}\beta', \tag{2}$$

$$xpol = {}^{\perp}\frac{(P(r)-B)r^2}{C_L O(r)} = {}^{\perp}\beta'. \tag{3}$$

The instrument also provides the total attenuated backscatter signal being the sum of the attenuated backscatter from all polarizations:

$$\beta' = {}^{\parallel}\beta' + {}^{\perp}\beta', \tag{4}$$

and the depolarization ratio being:

$$\delta = \frac{{}^{\perp}\beta'}{{}^{\parallel}\beta'}. \tag{5}$$

3 Methods

3.1 Background noise

The observed backscattered signal detected by a lidar consists of the true atmospheric signal and the background noise (Cao et al., 2013). The true atmospheric signal consists of backscattered contributions from particles (β_p) and molecular scattering (β_{mol}), whilst the background noise includes contributions from both solar radiation P_{solar} and instrument-related $P_{instrument}$

noise. Although the instrument already determines and performs the background correction internally, residual background components may still remain in the measured signal, as observed during termination hood measurements (see Sect 3.1.1). Therefore, we extend Eqs. 2 and 3 to account for background noise, B_{bk}, that is not removed by the internal correction:

$$ppol =^{\parallel} \frac{(P(r)-B)r^2}{C_L O(r)} +^{\parallel} \frac{B_{bk}(r)r^2}{C_L O(r)} =^{\parallel} \beta' +^{\parallel} \frac{B_{bk}(r)r^2}{C_L O(r)}, \tag{6}$$

$$xpol =^{\perp} \frac{(P(r)-B)r^2}{C_L O(r)} +^{\perp} \frac{B_{bk}(r)r^2}{C_L O(r)} =^{\perp} \beta' +^{\perp} \frac{B_{bk}(r)r^2}{C_L O(r)}. \tag{7}$$

To eliminate the range dependence from the background terms, we divide each expression by r^2, yielding:

$$\frac{ppol}{r^2} = \frac{^{\parallel}\beta'}{r^2} +^{\parallel} \frac{B_{bk}(r)}{C_L O(r)}, \tag{8}$$

$$\frac{xpol}{r^2} = \frac{^{\perp}\beta'}{r^2} +^{\perp} \frac{B_{bk}(r)}{C_L O(r)}. \tag{9}$$

For simplicity, we define the background terms as:

$$P_{bk}(r) \equiv \frac{B_{bk}(r)}{C_L O(r)}, \tag{10}$$

where $P_{bk}(r) = P_{solar}(r) + P_{instrument}(r)$.

Since the measured $ppol$ and $xpol$ signals include contributions from background noise in their respective polarization channels, it is necessary to estimate the background noise separately for each polarization. To achieve this, a background identification methodology has been developed. It identifies regions within the dataset that are free of aerosols and hydrometeors, where the $ppol$ and $xpol$ values are assumed to predominantly represent background noise.

The methodology proceeds as follows. First, the data is averaged over 5-minute intervals. The $\frac{ppol}{r^2}$ and $\frac{xpol}{r^2}$ profiles are then decomposed using the stationary wavelet transform (SWT) with the bior.1 wavelet, implemented via PyWavelets (Nason and Silverman, 1995; Lee et al., 2019). Subsequently, noise variance is reduced by applying a hard-threshold shrinkage function to the approximation and detail coefficients from levels 1 through 7, using minimax thresholding (Nason and Silverman, 1995). The profile is reconstructed via the inverse stationary wavelet transform. Finally, the noise range gates are identified as regions with values below half of the previously computed minimax threshold.

An example of this methodology applied to data in Kenttärova on 2024-03-28 is illustrated in Fig. 1. During daylight hours, solar radiation significantly increases the variance of the background noise in both $\frac{ppol}{r^2}$ and $\frac{xpol}{r^2}$, resulting in a daytime variance much higher than that observed at night, as shown in panels (g) and (h). Above the aerosol and cloud layers, both the mean and variance of the background $\frac{ppol}{r^2}$ and $\frac{xpol}{r^2}$ signals remain relatively stable with range, or at least exhibit considerably smaller variations compared to the diurnal fluctuations.

By applying this methodology to the full dataset, we obtained the time series of $P_{bk}(r)$ for all instruments in both polarizations. Comparing these background noise levels with other housekeeping parameters, such as laser power, enables us to evaluate the operational performance of each instrument. Moreover, since each noise component is quantified independently,

https://doi.org/10.5194/egusphere-2025-6331
Preprint. Discussion started: 4 January 2026

we can correct the signal and estimate its uncertainty in both polarization $ppol$ and $xpol$ and, consequently, in the derived depolarization ratio.

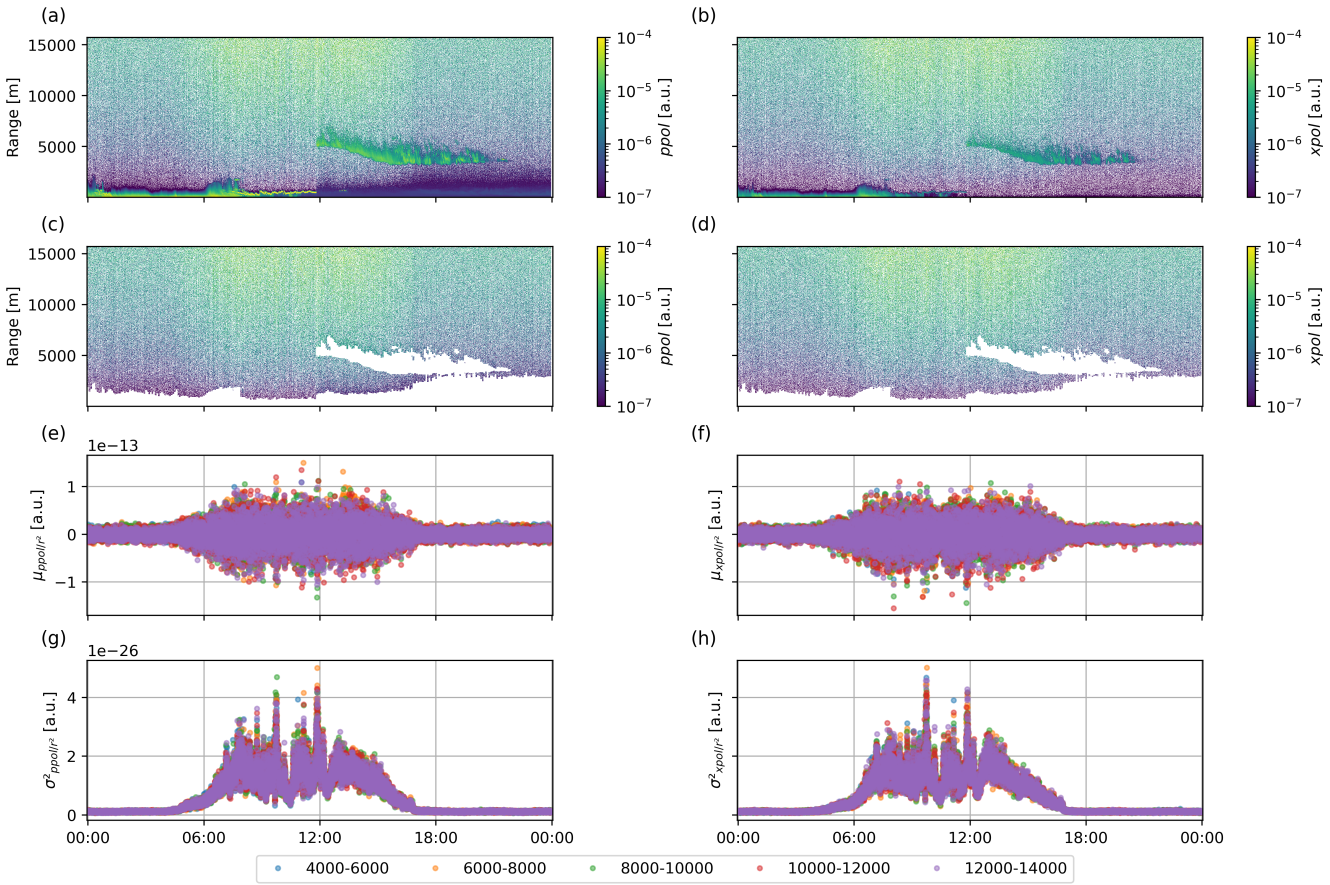

Figure 1. Time series from Kenttärova on 2024-03-28 showing: a) $ppol$, b) $xpol$, c) background $ppol$, and d) background $xpol$. Subplots e–h display the background signals at different range bins from $4000-6000\,\mathrm{m}$, $6000-8000\,\mathrm{m}$, $8000-10000\,\mathrm{m}$, $10000-12000\,\mathrm{m}$, $120000-14000\,\mathrm{m}$, with color indicating the range bin: e) μ_{ppol}, f) μ_{xpol}, g) $\sigma^2{}_{ppol}$, and h) $\sigma^2{}_{xpol}$. These parameters are computed at a 10-second temporal resolution using all data within each range bin.

3.1.1 Instrumental noise

Figure 2. A termination hood (Vaisala CL61TERMHOOD) place on top of the CL61 in Hyytiala

To obtain the instrument's noise level, a termination hood (Vaisala CL61TERMHOOD) was placed over the window of each ceilometer located in Finland. The hood was applied without notifying the instrument, so that it operated as it would under normal conditions. The hood's material and design totally attenuate the outgoing laser beam, preventing any backscatter signal from reaching the detector. As a result, the measured signal can be attributed entirely to the instrumental noise term, i.e. $\frac{ppol}{r^2} =^{\parallel} P_{instrument}(r)$, $\frac{xpol}{r^2} =^{\perp} P_{instrument}(r)$ during the termination hood measurement.

Figure 3 presents example profiles of $ppol$ and $xpol$ both before and during the termination hood measurements. Before the termination hood was applied, the μ_{ppol} and μ_{xpol} profiles in the aerosol and hydrometeor-free region above $5\ \mathrm{km}$ closely follow the theoretical molecular backscatter β_{mol} (Fig. 3b and c), indicating that the CL61 ceilometer is sensitive to molecular scattering. The method for calculating β_{mol} is described in the following section. At ranges above $10\ \mathrm{km}$, however, the molecular signal becomes indistinguishable from noise. The standard deviation profiles, σ_{ppol/r^2} and σ_{xpol/r^2}, also remain relatively constant in this region (Fig. 3f and g).

During the termination hood measurement, the instrumental noise profiles $P_{instrument}(r)$ remain relatively stable above $1.2\ \mathrm{km}$, but increase significantly below this range (Figs. 3d, e, h, and i). This increase indicates a signal bias at lower ranges. Additionally, a reduction in the standard deviation of both polarization channels is observed during the termination hood measurement compared to the period before. This reduction is attributed to the absence of solar influence during the termination hood measurement.

Since the CL61 ceilometer is a coaxial lidar, it is prone to the afterpulsing effect, such as those caused by internal reflections of the outgoing laser beam that reach the detector (Campbell et al., 2002; Welton and Campbell, 2002). Additionally, Hervo

https://doi.org/10.5194/egusphere-2025-6331
Preprint. Discussion started: 4 January 2026

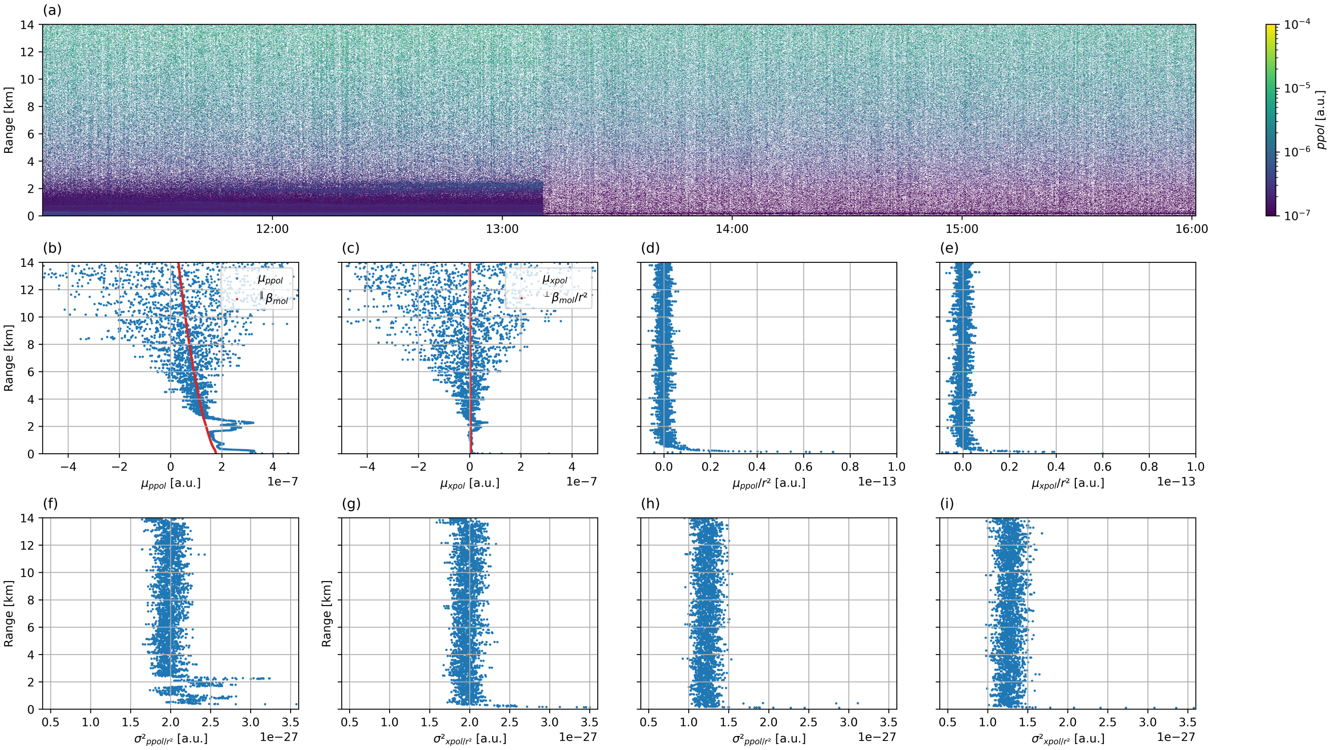

Figure 3. Measurements at Kenttärova on 5 March 2024. a) the time series of *ppol*. Panels b, c, f, g, display the averaged profiles in time at each range gate before the termination hood measurement (from 11 to 13 UTC): b) μ_{ppol} and $\| \beta_{mol}$, c) μ_{xpol} and $\perp \beta_{mol}$, f) σ_{ppol/r^2}, g) σ_{xpol/r^2}. Panels d, e, h, i, display the averaged profiles in time at each range gate during the termination hood measurement at 19 °C (from 14 to 15 UTC): d) μ_{ppol/r^2} , e) μ_{xpol/r^2}, h) $\sigma_{ppol/r^2}/$, i) σ_{xpol}/r^2.

et al. (2016) demonstrated that the overlap function for a ceilometer made by another manufacturer (Lufft CHM15k) was sensitive to the instrument internal temperature, T, mainly due to temperature-induced changes in its optical components. Although Vaisala does apply a correction for the overlap function, it is likely that this is a time-invariant correction and that the bias observed is due to the combined effects of changes in afterpulsing and the possible temperature dependence of the overlap correction. To quantify this effect, the termination hood measurement was repeated for a range of T over a two-year period. This approach enabled the derivation of $^{\|}P_{instrument}(r,T)$ and $^{\perp}P_{instrument}(r,T)$, i.e. w.r.t. to T.

3.1.2 Solar noise

For an accurate estimation of background noise, the contribution from solar radiation must be taken into account. The solar noise variance can be seen from the diurnal pattern in Fig. 3 and the difference between the σ^2 profiles before and during the termination hood measurement in Fig. 3f, g, h and i. Since this difference remains approximately constant at all ranges above the aerosol layer near the ground, we assume that the solar noise variance from both polarizations, $\sigma^2{}_{P_{solar}}$, is also uniform down to the near range. $\sigma^2{}_{P_{solar}}$ is then calculated by computing the difference between the total background noise variance $\sigma^2{}_{P_{bk}}$ (obtained between 10 to 12 km using the background identification methodology) and the instrumental noise variance $\sigma^2{}_{P_{instrument}}$ (obtained at the same range and temperature from the termination hood measurement):

$$\sigma^2{}_{P_{solar}} = \sigma^2{}_{P_{bk}(r=10-12km)} - \sigma^2{}_{P_{instrument}(r=10-12km,T)}. \tag{11}$$

Here, $\sigma^2_{P_{\mathrm{solar}}}$ is independent of the range and obtained separately for each polarization.

As noted by Kotthaus et al. (2016), earlier instruments such as the CL31 incorporate a zero-bias level that compensates for temporal fluctuations in solar radiation. This is also evident in CL61 as shown in Fig. 2b and 2c, where the μ_{ppol} and μ_{xpol} values above 5 km closely follow β_{mol}, confirming the zero-mean solar radiation noise.

3.1.3 Correction for systematic bias

After measuring $P_{instrument}(r,T)$ across a range of T during the termination hood measurements, the results are stored as a lookup table containing $P_{instrument}(r,T)$ profiles at each T. The attenuated backscatter for each polarization can be corrected by applying the $P_{instrument}(r,T)$ value corresponding to the instrument's current internal temperature as follows:

$$^{\parallel}\beta' = ppol - \mu_{^{\parallel}P_{instrument}(r,T)}r^2, \tag{12}$$

$$^{\perp}\beta' = xpol - \mu_{^{\perp}P_{instrument}(r,T)}r^2, \tag{13}$$

and their corresponding uncertainties given by:

$$\sigma^2{}_{^{\parallel}\beta'} = (\sigma^2{}_{^{\parallel}P_{solar}} + \sigma^2{}_{^{\parallel}P_{instrument}(r,T)})r^2, \tag{14}$$

$$\sigma^2{}_{^{\perp}\beta'} = (\sigma^2{}_{^{\perp}P_{solar}} + \sigma^2{}_{^{\perp}P_{instrument}(r,T)})r^2. \tag{15}$$

The bias-corrected attenuated backscatter and depolarization ratio are then calculated as:

$$\beta'_{corrected} =^{\parallel} \beta' +^{\perp} \beta', \tag{16}$$

$$\delta_{corrected} = \frac{^{\perp}\beta'}{^{\parallel}\beta'}, \tag{17}$$

and their associated uncertainty, given by

$$\sigma^2{}_{\beta'_{corrected}} = \sigma^2{}_{^{\parallel}\beta'} + \sigma^2{}_{^{\perp}\beta'}, \tag{18}$$

$$\sigma^2{}_{\delta_{corrected}} = \delta^2\left(\frac{\sigma^2{}_{^{\perp}\beta'}}{^{\perp}\beta'^2} + \frac{\sigma^2{}_{^{\parallel}\beta'}}{^{\parallel}\beta'^2}\right). \tag{19}$$

3.2 Calibration

To ensure the CL61 produces a consistent and accurate backscatter signal, the ceilometer signal must be manually calibrated in addition to its internal calibration. This involves calibrating the backscatter signal from the CL61 using a reference target

https://doi.org/10.5194/egusphere-2025-6331
Preprint. Discussion started: 4 January 2026

with known backscatter characteristics. Two commonly used calibration methods for deriving C_L are based on different types of reference targets: atmospheric molecules (Rayleigh calibration) and liquid clouds (liquid cloud calibration).

The Rayleigh calibration (Fernald et al., 1972; Klett, 1985; Binietoglou et al., 2011; Wiegner and Geiß, 2012; Baars et al., 2016), often referred to as the backward inversion approach, is the standard method to derive the aerosol particle backscatter coefficient (β_p) for most research aerosol lidars due to their sensitivity to molecular signal (Wiegner et al., 2014). As illustrated in Fig. 3b, the attenuated backscatter coefficient profile from CL61 closely follows the attenuated molecular backscatter coefficient above the aerosol layer at $4\ \mathrm{km}$. This indicates a significant contribution of molecular scattering to the total CL61 signal, especially in aerosol- and hydrometeor-free regions. Therefore, the Rayleigh calibration can be applied to the CL61, provided a sufficiently long averaging time (more than 2 hours) is used.

The Rayleigh calibration method requires an assumed lidar ratio for aerosol particles (S_p). At sites equipped with a sun photometer, S_p can be constrained (Wiegner and Geiß, 2012); otherwise, a value of $50\ \mathrm{sr}$ was used. Additionally, the β_m profile is needed for the inversion and was calculated following the method described by Bucholtz (1995) using meteorological input data from a numerical weather prediction model available from the ACTRIS Cloudnet data portal (O'Connor, 2025). After the β_p profile is derived, the lidar constant C_L can be determined from the lidar equation (Wiegner and Geiß, 2012).

The liquid cloud calibration (O'Connor et al., 2004; Hopkin et al., 2019) relies on the fact that the lidar ratio for liquid water clouds at the ceilometer wavelength is known. This method involves calculating the integrated attenuated backscatter coefficient for fully attenuated liquid water clouds, including the contribution from multiple scattering. The theoretical contribution from multiple scattering is computed for droplet diameters ranging from 8 to 20 $\mu\mathrm{m}$ and with the CL61 beam divergence and receiver field of view. The integrated backscatter coefficient is then scaled to fit within the expected theoretical values and this scaling factor is the calibration factor C, which is the reciprocal of the lidar constant C_L. The primary advantage of this approach over Rayleigh calibration is the substantially higher signal-to-noise ratio of the backscatter from water clouds compared to the molecular backscatter. As a result, it eliminates the need for long nighttime averaging periods required to obtain a reliable molecular signal.

A methodology was developed to identify suitable liquid cloud profiles. First, an example liquid cloud profile is chosen as a reference. Then, each profile is cross-correlated with this reference to quantify their similarity. For each time step, the profile with the highest cross-correlation value is considered the most similar. Additionally, a liquid cloud profile is then selected if the proportion of in-cloud β' to the sum of the profile β' exceeds 90% as this ensures that the integrated β' is not impacted by strong aerosol or precipitation.

To ensure robust data fitting, the cloud calibration is performed monthly using all suitable liquid cloud observations detected from the methodology. To validate the cloud calibration results, Rayleigh calibration was also computed occasionally when possible. Data from a co-located sun photometer was used to constrain the lidar ratio for Rayleigh calibration. If no sun photometer data is available, a lidar ratio of $50\ \mathrm{sr}$ is used.

The calibrated volume attenuated backscatter coefficient and its uncertainty can then be determined as:

$$\beta'_v = \beta'_{corrected} \cdot C, \tag{20}$$

$$\sigma^2{}_{\beta'_v} = \sigma^2{}_{\beta'_{corrected}} \cdot C^2. \tag{21}$$

For those instruments where terminal hood measurements are not available:

$$\beta'_v = \beta' \cdot C, \tag{22}$$

$$\sigma_{\beta'_v} = \sigma^2{}_{P_{solar}} \cdot C^2 = (\sigma^2{}_{\parallel P_{solar}} + \sigma^2{}_{\perp P_{solar}}) \cdot C^2. \tag{23}$$

The calibration is assumed to affect both polarization channels equally. Hence, δ remains unchanged.

3.3 Aerosol particle inversion

The aerosol particle backscatter coefficient profile (β_p) is retrieved using the forward Klett solution (Klett, 1985) after applying the previously derived cloud calibration factor and assuming that the instrument does not undergo significant degradation within a one-month period. The cloud calibration factor is estimated to have an uncertainty of approximately 10% (Hopkin et al., 2019). The forward inversion does not require extensive temporal averaging. When available, sun photometer observations are used to constrain the lidar ratio S_p; otherwise, a constant value of 50 sr is applied to all aerosol layers in the retrieval.

Let $\beta_p = f(\beta'_v, C, S_p)$ represent the inversion function; then the uncertainty of β_p is calculated as

$$\sigma^2_{\beta_p} = \left(\frac{\partial f}{\partial \beta'_v}\sigma_{\beta'_v}\right)^2 + \left(\frac{\partial f}{\partial C}\sigma_C\right)^2 + \left(\frac{\partial f}{\partial S}\sigma_S\right)^2. \tag{24}$$

The partial derivatives can be approximated using central differences:

$$\frac{\partial f}{\partial \beta'_v}\sigma_{\beta'_v} \approx \frac{f(\beta'_v + \sigma_{\beta'_v}, C, S_p) - f(\beta'_v - \sigma_{\beta'_v}, C, S_p)}{2}, \tag{25}$$

$$\frac{\partial f}{\partial C}\sigma_C \approx \frac{f(\beta'_v, C_{\max}, S_p) - f(\beta'_v, C_{\min}, S_p)}{2}, \tag{26}$$

$$\frac{\partial f}{\partial S}\sigma_{S_p} \approx \frac{f(\beta'_v, C, S_{p,\max}) - f(\beta'_v, C, S_{p,\min})}{2}. \tag{27}$$

with $C_{min} = 0.9 \cdot C$, $C_{max} = 1.1 \cdot C$, $S_{p,\min} = S_p - 10$ and $S_{p,\min} = S_p + 10$

Following (Biele et al., 2000; Freudenthaler et al., 2009), the particle depolarization ratio (δ_p) is then obtained as

$$\delta_p = \frac{(1+\delta_m)\delta_v R - (1+\delta_v)\delta_m}{(1+\delta_m)R - (1+\delta_v)}, \tag{28}$$

where the backscatter ratio R is defined as

$$R = \frac{\beta_p + \beta_m}{\beta_m}, \tag{29}$$

and δ_v is the volume depolarization ratio, which is $\delta_{corrected}$ in Eq. 17 or $\frac{xpol}{ppol}$ for instruments lacking terminal hood measurements.

https://doi.org/10.5194/egusphere-2025-6331
Preprint. Discussion started: 4 January 2026

The molecular depolarization ratio (δ_m) is estimated following Tomasi et al. (2005), accounting for major atmospheric gases and the influence of water vapor. The input data for these calculations are taken from a numerical weather prediction model provided via the ACTRIS Cloudnet data portal (O'Connor, 2024).

The uncertainty of δ_p can be determined using partial derivatives

$$\sigma_{\delta_p}^2 = \left(\frac{\partial \delta_p}{\partial \delta_m}\sigma_{\delta_m}\right)^2 + \left(\frac{\partial \delta_p}{\partial \delta_v}\sigma_{\delta_v}\right)^2 + \left(\frac{\partial \delta_p}{\partial R}\sigma_R\right)^2. \tag{30}$$

Assuming σ_{β_m} and σ_{δ_m} are negligible and approximating $\sigma_R \approx \sigma_{\beta_p}$, this reduces to

$$\sigma_{\delta_p}^2 \approx \left(\frac{\partial \delta_p}{\partial \delta_v}\sigma_{\delta_v}\right)^2 + \left(\frac{\partial \delta_p}{\partial R}\sigma_{\beta_p}\right)^2. \tag{31}$$

The partial derivatives are calculated as:

$$\frac{\partial \delta_p}{\partial \delta_v} = \frac{(1+\delta_m)^2 R(R-1)}{((1+\delta_m)R-(1+\delta_v))^2}, \tag{32}$$

$$\frac{\partial \delta_p}{\partial R} = \frac{(1+\delta_m)(1+\delta_v)(\delta_m-\delta_v)}{((1+\delta_m)R-(1+\delta_v))^2}. \tag{33}$$

https://doi.org/10.5194/egusphere-2025-6331
Preprint. Discussion started: 4 January 2026

4 Results and discussion

4.1 Background noise

Figure 4 shows the time series of background noise, normalized by integration time, alongside the laser power. Most instruments (except for Vehmasmäki) exhibit a gradual decline in laser power, accompanied by corresponding increases in background noise. These changes often occur in discrete steps rather than as a continuous trend. Notably, fluctuations in background noise are consistently related to changes in laser power. Periods of restored laser power and decreased background noise align with documented hardware interventions, such as transmitter replacements at Vehmasmäki (Dec 2022; Fig. 4a) and Hyytiälä (Feb 2024; Fig. 4b).

At Hyytiälä and Kenttärova, laser power gradually decreases from 100% to around 40% over two years. In contrast, the CL61 at Vehmasmäki maintains a consistently high laser power, ranging between 90% and 100% throughout the same period, with only a slight decrease during the summer, likely to regulate the internal temperature to prevent overheating. Meanwhile, the CL61 at Lindenberg experienced a sharp decline in laser power, from 80% to below 10% within just one year of operation. We also found that changes in the firmware version do not appear to have any noticeable effect on background noise levels.

The relationship between background noise, normalized by integration time, and laser power across several instruments is illustrated in Fig. 5. Nighttime measurements (23:00 to 01:00 local time), shown in blue, are unaffected by solar radiation, while all-day measurements are displayed in grey. It is important to note that the selected nighttime window is arbitrary and used solely for this analysis; for instance, locations such as Kenttärova experience no true nighttime during summer. The nighttime data clearly indicate that a decrease in laser power leads to an increase in background noise across all instruments. Daytime background noise is generally higher due to solar radiation, which varies with factors such as solar angle, cloud height, and surface albedo, making direct comparisons more complex. Nevertheless, the figure suggests that lower laser power also contributes to increased noise levels during daytime conditions.

An increase in background noise can significantly reduce an instrument's ability to detect weak aerosol signals. This effect is clearly illustrated in Fig. S1 in the supplement. On 7 March 2024, an elevated aerosol layer was observed above $3\,\mathrm{km}$ in Lindenberg, indicated by enhanced attenuated backscatter coefficient values compared to those at lower altitudes between $1-3\,\mathrm{km}$ (Fig. S1a, c). However, by 2 December, 2024, a reduction in laser power led to a higher noise floor which meant that if a similar aerosol layer were present, it would no longer be distinguishable from the background noise (Fig. S1b, c).

https://doi.org/10.5194/egusphere-2025-6331
Preprint. Discussion started: 4 January 2026

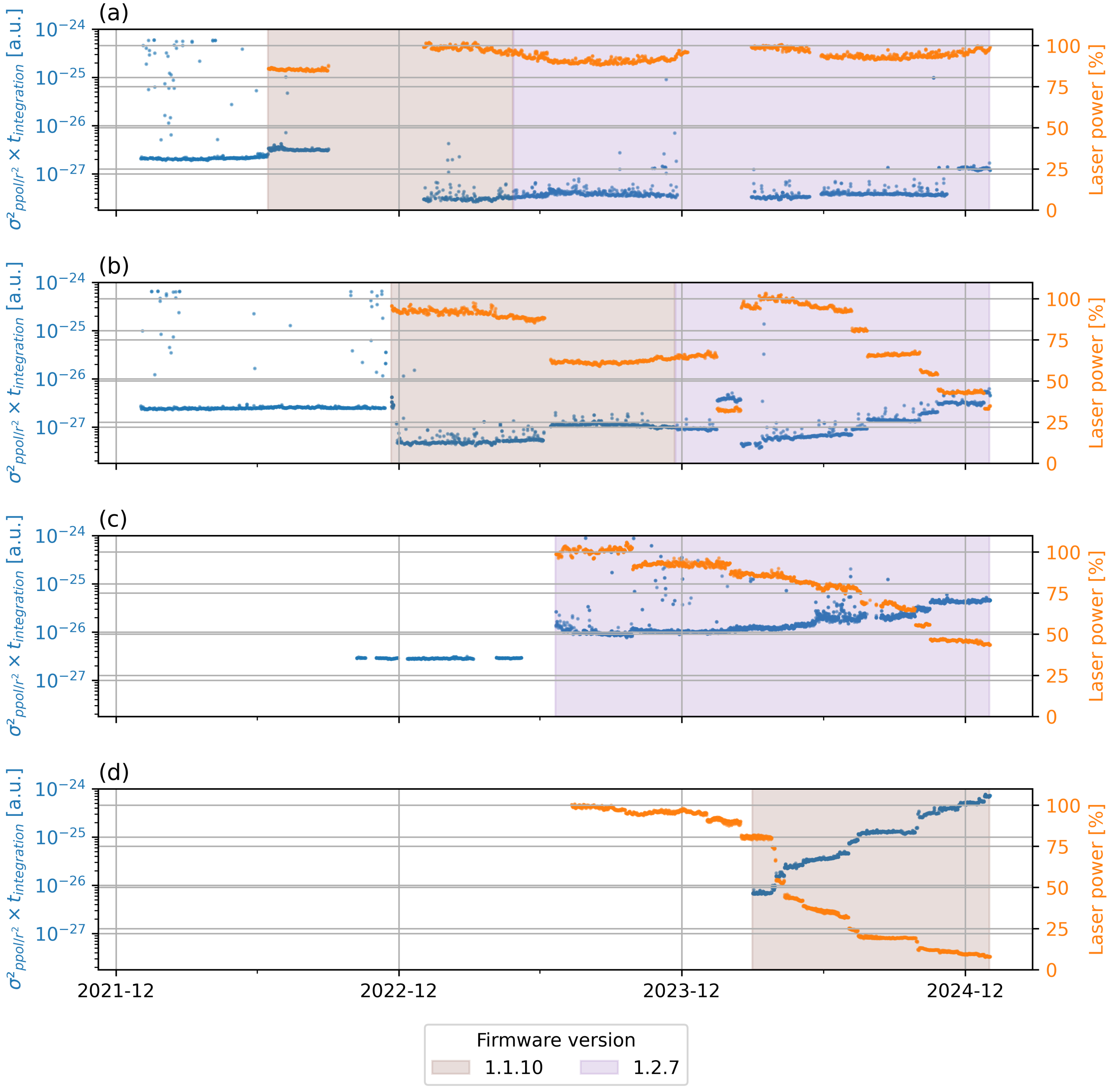

Figure 4. Time series of nighttime background noise variance normalized by the integration time ($\sigma^2_{ppol/r^2} \times t_{intergration}$), and the laser power are shown for (a) Vehmasmäki, (b) Hyytiälä, (c) Kenttärova, and (d) Lindenberg. Shaded regions denote different firmware versions; unshaded areas represent periods with no recorded firmware version and laser power.

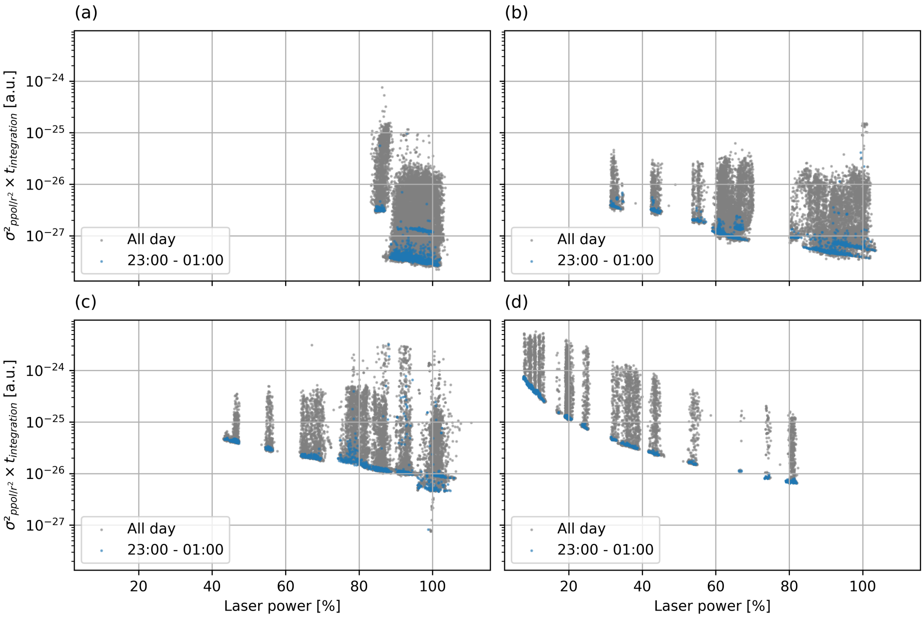

Figure 5. Variance of background noise as a function of laser power percentage, normalized by integration time, at the following locations: a) Vehmasmäki, b) Hyytiälä, c) Kenttärova, and d) Lindenberg. Blue points represent data collected during nighttime hours (23:00–01:00 local time), while grey points include all available data.

https://doi.org/10.5194/egusphere-2025-6331
Preprint. Discussion started: 4 January 2026

4.2 Instrumental noise

In this section, we examine how the instrumental bias (μ_{ppol/r^2}, μ_{xpol/r^2}) and noise (σ^2_{ppol/r^2}, σ^2_{xpol/r^2}), obtained during the termination hood measurement, vary with temperature and over time. The termination hood measurement was deployed multiple times at Vehmasmäki, Hyytiälä, and Kenttärova. Figure 6 presents the instrumental noise profiles recorded during these termination hood measurement periods, which have been averaged and grouped according to the instruments' internal temperatures.

For the instruments located in Hyytiälä and Kenttärova, the μ_{ppol/r^2} values remain relatively stable around zero from the far range down to about 2 km, then increase sharply as the range decreases. On the other hand, the instrument in Vehmasmäki also remains near zero at far range, but its μ_{ppol/r^2} begins to increase around 5 km and continues to rise toward shorter ranges. Meanwhile, the μ_{xpol/r^2} profiles for all three instruments remain near zero from the far range to about 2 km, after which they increase rapidly with decreasing range.

Overall, the internal temperature T has a more pronounced effect on the mean instrumental noise profiles below 1 km than at higher ranges. In particular, both μ_{ppol/r^2} and μ_{xpol/r^2} profiles deviate substantially from zero below 200 m (see Fig. 7) across all instruments. Notably, each instrument shows the same small peak in both μ_{ppol/r^2} and μ_{xpol/r^2} profiles at approximately 150 m.

All instruments exhibit profiles of σ^2_{ppol/r^2} and σ^2_{xpol/r^2} which are constant above 500 m, followed by a sharp increase below this range. These variance profiles show a pronounced sensitivity to internal temperature, with lower temperatures producing higher σ_{ppol/r^2} and σ_{xpol/r^2} throughout the entire range.

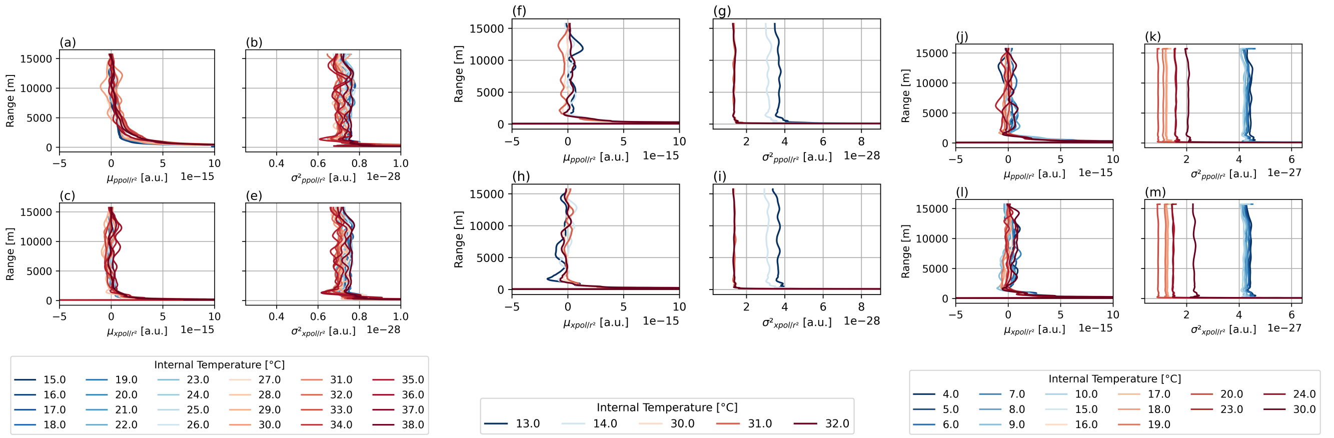

Figure 6. Termination hood profiles at various internal temperatures (color-coded) across different sites. In Vehmasmaki: a) μ_{ppol/r^2}, b) σ_{ppol/r^2}, c) μ_{xpol/r^2}, and d) σ_{xpol/r^2}. In Hyytiala: f) μ_{ppol/r^2}, g) σ_{ppol/r^2}, h) μ_{xpol/r^2}, and i) σ_{xpol/r^2}. In Kenttärova: j) μ_{ppol/r^2}, k) σ_{ppol/r^2}, l) μ_{xpol/r^2}, and m) σ_{xpol/r^2}

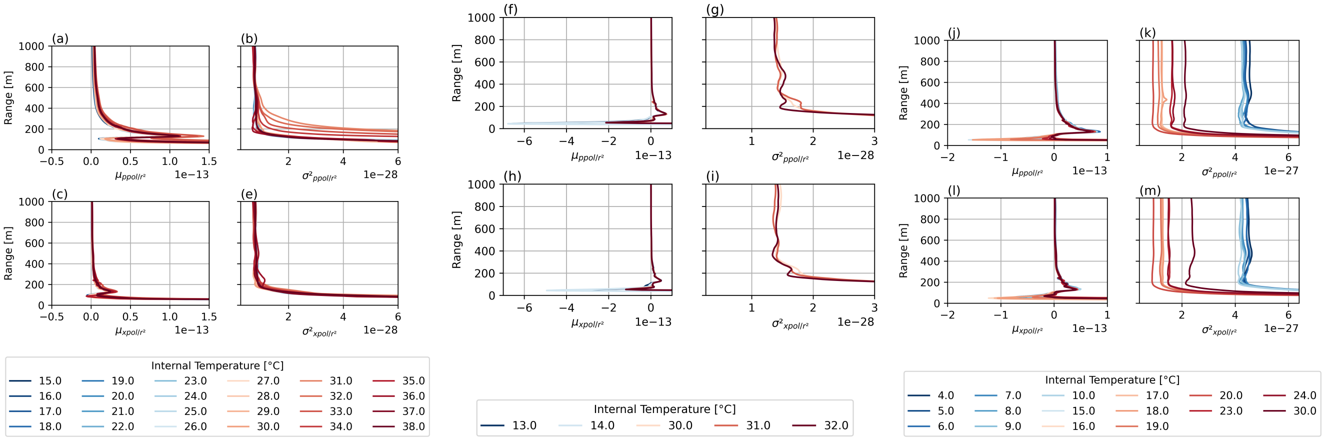

Figure 7. Termination hood profiles at various internal temperatures (color-coded) across different sites only up to 1000 m range. In Vehmasmaki: a) μ_{ppol/r^2}, b) σ_{ppol/r^2}, c) μ_{xpol/r^2}, and d) σ_{xpol/r^2}. In Hyytiala: f) μ_{ppol/r^2}, g) σ_{ppol/r^2}, h) μ_{xpol/r^2}, and i) σ_{xpol/r^2}. In Kenttärova: j) μ_{ppol/r^2}, k) σ_{ppol/r^2}, l) μ_{xpol/r^2}, and m) σ_{xpol/r^2}.

For all instruments, the signal near the surface exhibits much more rapid fluctuations than at higher range gates. Figure S2 displays example profiles of $ppol$, $xpol$, and the instrument's internal temperature during a termination hood measurement at Kenttärova, revealing periodic variations in the signal below 50 m. To investigate this, the Fourier transforms of these signals were computed at each range gate over time and compared to that of the laser temperature recorded simultaneously. The results show that both the signals and the laser temperature exhibit a coincident spectral peak at approximately 0.0079 Hz (about 120 s), indicating a strong influence of laser temperature on the signals. Furthermore, additional distinct peaks in the signal spectra imply the presence of other instrument-related effects. Overall, these periodic variations appear sporadically across all instruments, with no consistent pattern indicating when they appear or disappear. Given the difficulty in developing a reliable correction method, we recommend excluding measurements below 50 m.

Figure S3 in the supplement shows how the instrumental bias during the termination hood measurement at Vehmasmäki varies over time under consistent internal temperature conditions. Overall, calibration profiles at a fixed internal temperature remain consistent for at least one month, but small deviations can emerge over a six-month period. As a result, we recommend performing the termination hood measurement checks every few months during continuous operation.

https://doi.org/10.5194/egusphere-2025-6331
Preprint. Discussion started: 4 January 2026

4.3 Calibration

Figure 8 presents the time series of calibration factor from the cloud calibration and Rayleigh calibration methods for all the ceilometers. Detailed results of the cloud calibration factors derived from liquid cloud signals at each site are presented in Figures S4–S7. Overall, the calibration factors obtained from the two methods agree well within their respective uncertainties, In Lindenberg, the calibration factor from the cloud calibration exhibits an approximate threefold decline over time, reflecting notable signal degradation. During this degradation period, Rayleigh calibration could not be performed because the elevated background-noise level (see Section 4.1) obscured the molecular return. In contrast, the other instruments show only short-term fluctuations without any clear long-term trend. Two periods with notable deviations in the calibration factor were also identified: June to October 2023 and November to December 2024 in Vehmasmäki. The issue in the CL61 ceilometer at Vehmasmäki is due to the fogged window that attenuates the outgoing signal. This will be analyzed in more detail in the following section.

Across all instruments, the calibration factor generally stays within the range of 0.9 to 1.5 as long as laser power remains above 40%, aside from occasional deviations due to specific instrument issues. In Vehmasmaki, as the laser power remains above 90%, the calibration factor fluctuates around 1 within 10% fluctuation. In Hyytiala, the highest changes in calibration factor is observed when the instrument below 80% with the firmware $1.1.10$ and then below 60% with the firmware $1.2.7$. However, the calibration factor remains relatively stable at 1.25 even when the laser power drops from 100% to 40% with the firmware 1.2.7. In Kenttärova, laser power percentages were not recorded before June 2023, but the observed increase in the calibration factor is likely linked to a decrease in laser power. After a new transmitter was installed, the calibration factor returned to around 1. In Lindenberg, a noticeable decline in the cloud calibration factor was observed as laser power dropped from 40% to 10%. It is still to be ascertained whether this trend also appears in instruments running the newer firmware version 1.2.7.

Figure S8 demonstrates the utility of cloud calibration for two cases; one with 80% laser power on 2024-03-03 and another with just 10% on 2024-11-16. This indicates that the method can still be used in situations with low laser power and since the internal calibration value may not scale with low laser power values, regular cloud calibration is necessary to understand instrument performance and continue to provide profiles that can be used quantitatively, especially for laser power values below 40%.

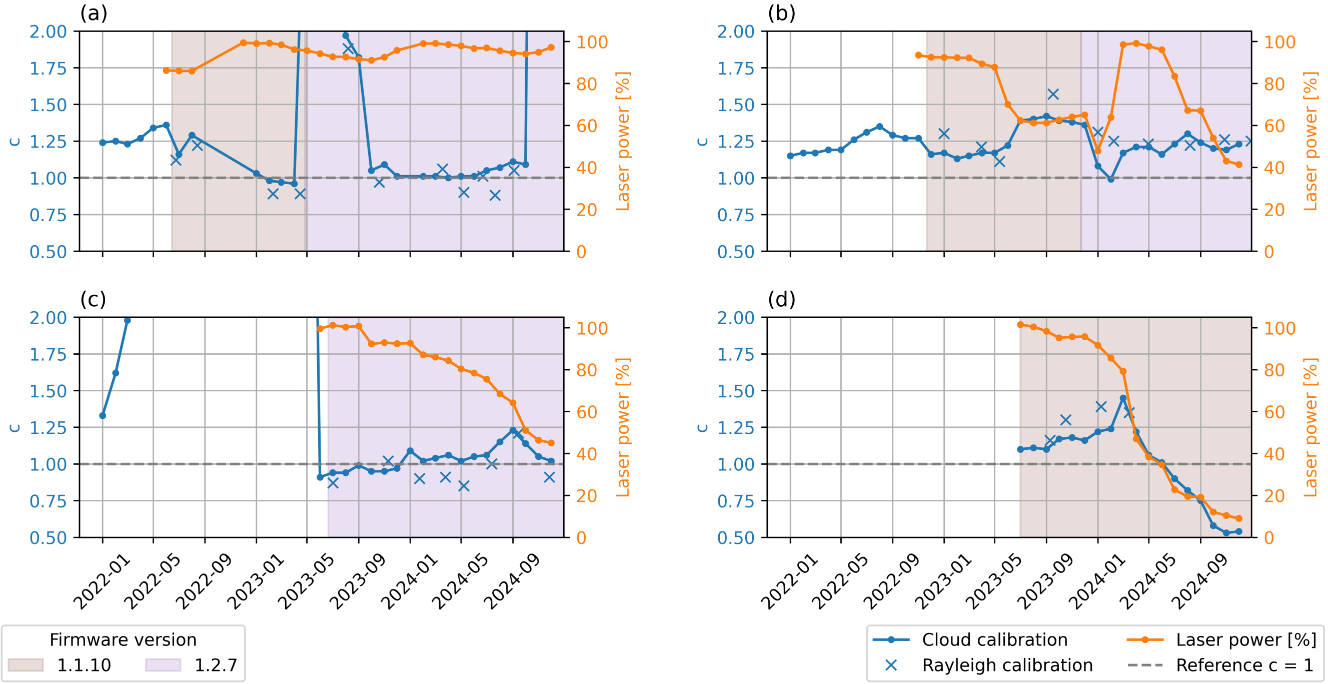

Figure 8. Time series of the calibration factor from cloud calibration, Rayleigh calibration and laser power at four sites: a) Vehmasmäki, b) Hyytiälä, c) Kenttärova, and d) Lindenberg. The dashed line indicates a calibration factor of $c = 1$. Periods corresponding to different firmware versions are highlighted with shaded areas.

https://doi.org/10.5194/egusphere-2025-6331
Preprint. Discussion started: 4 January 2026

4.4 Signal correction and uncertainty estimation

After recording the termination hood profiles at different temperatures and determining the calibration factor, the correction and forward Klett inversion can be applied, and the associated uncertainty can be estimated using the method described in Sect. 3.3. Example results of this procedure are illustrated in Figs. 9 and 10. During this period, the calibration factor was close to 1. On this date (Fig. 10), aerosol was present below $1000\ \mathrm{m}$ within the boundary layer close to the ground, while several layers of clouds extended from $2\ \mathrm{km}$ up to $3.5\ \mathrm{km}$. Fig. 9 presents the β, δ and their associated uncertainties in the aerosol layer below $1000\ \mathrm{m}$ obtained in the same day at 13:00 UTC.

In this range, the instrument bias-corrected β_v differs only slightly from the original uncorrected β, with values ranging from 1×10^{-9} to $2.5 \times 10^{-9}\ \mathrm{sr}^{-1}\ \mathrm{m}^{-1}$ (Fig. 9a). This difference is expected to be even smaller within the clouds, where the signal is stronger and the instrumental bias decreases with increasing range. In contrast, the aerosol backscatter β_p is substantially lower than β by approximately $1.5 \times 10^{-7}\ \mathrm{sr}^{-1}\ \mathrm{m}^{-1}$, indicating a significant contribution from molecular scattering. The $\sigma^2_{\beta_v}$ and $\sigma^2_{\beta_p}$ profiles are relatively similar to each other, and they both increase exponentially with height (Fig. 9b).

Similarly, the original uncorrected (δ) and the instrument bias corrected (δ_v) profiles differ only slightly, by about 0.001 to 0.005 (Fig. 9c). In contrast, the aerosol depolarization ratio δ_p is substantially higher, differing from the original δ by approximately 0.1. The variances ($\sigma^2_{\delta_v}$, $\sigma^2_{\delta_p}$) are comparable below $200\ \mathrm{m}$, but at higher ranges, $\sigma^2_{\delta_p}$ becomes markedly larger.

Overall, the pronounced differences between β and β_p, as well as between δ and δ_p, highlight the importance of accounting for the molecular contribution when performing quantitative assessments of aerosol measurement with this instrument. While the difference between β and β_v (and δ and δ_v) may be small, the hood termination remains important as it allows the estimation of measurement uncertainty.

Figure 10 illustrates the time series of β_v, δ_v, β_p, and δ_p profiles, along with their corresponding variances on the same day. Similar to Fig. 9, β_v is higher than β_p while δ_v is lower than β_p in this period. The profiles of $\sigma^2_{\beta_v}$ and $\sigma^2_{\beta_p}$ vary with time during this period, with an exponential increase with range. On the other hand, the $\sigma^2_{\delta_v}$ and $\sigma^2_{\delta_p}$ profiles demonstrate a more pronounced dependence on the signal magnitude (Fig. 10 d and h).

https://doi.org/10.5194/egusphere-2025-6331
Preprint. Discussion started: 4 January 2026

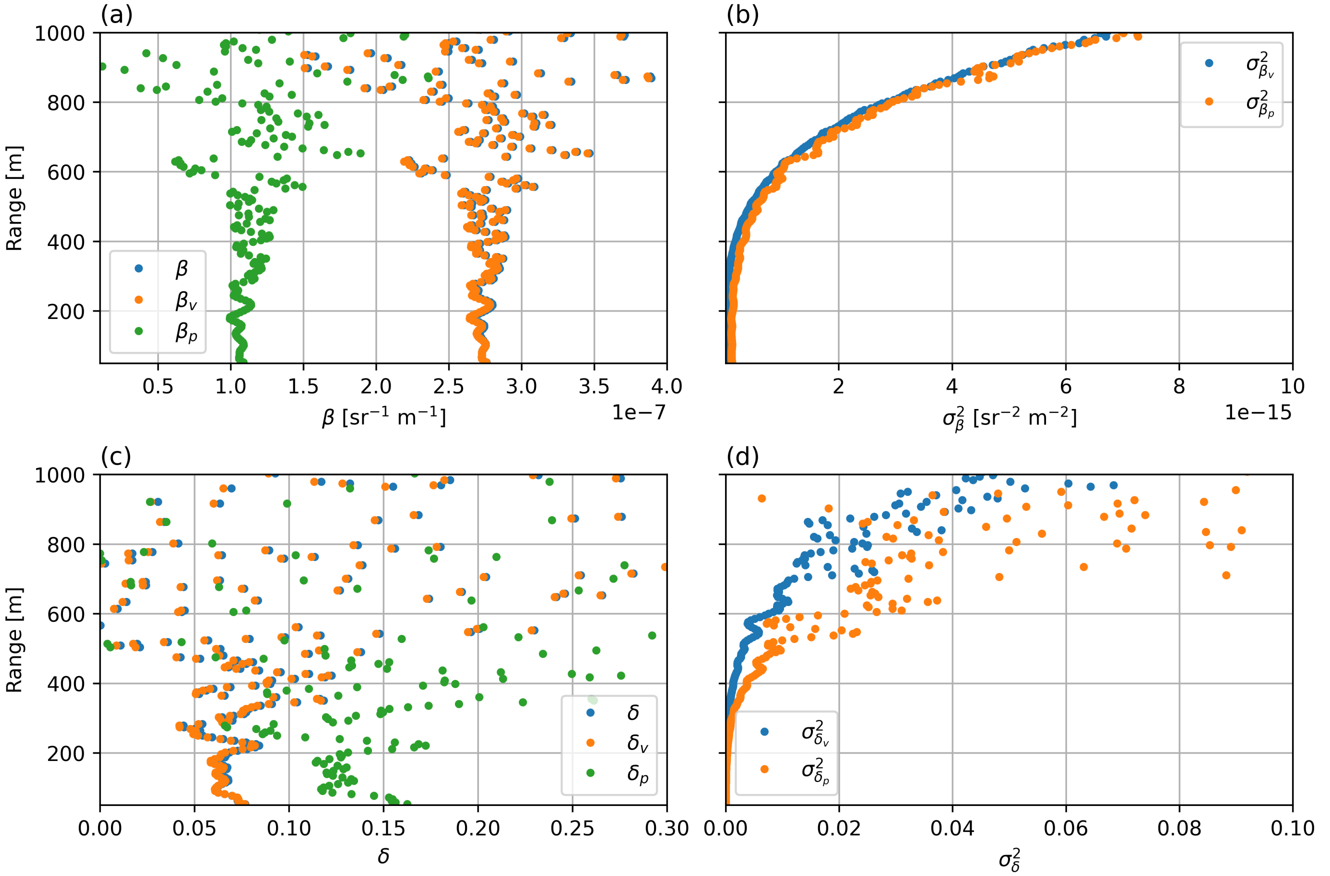

Figure 9. Example of uncorrected and corrected profiles in Kenttarova measured at 2024-06-04 13:01 UTC. a) β, β_v, β_p, b) $\sigma^2_{\beta_v}$, $\sigma^2_{\beta_p}$, c) δ, δ_v, δ_p, d) $\sigma^2_{\delta_v}$, $\sigma^2_{\delta_p}$.

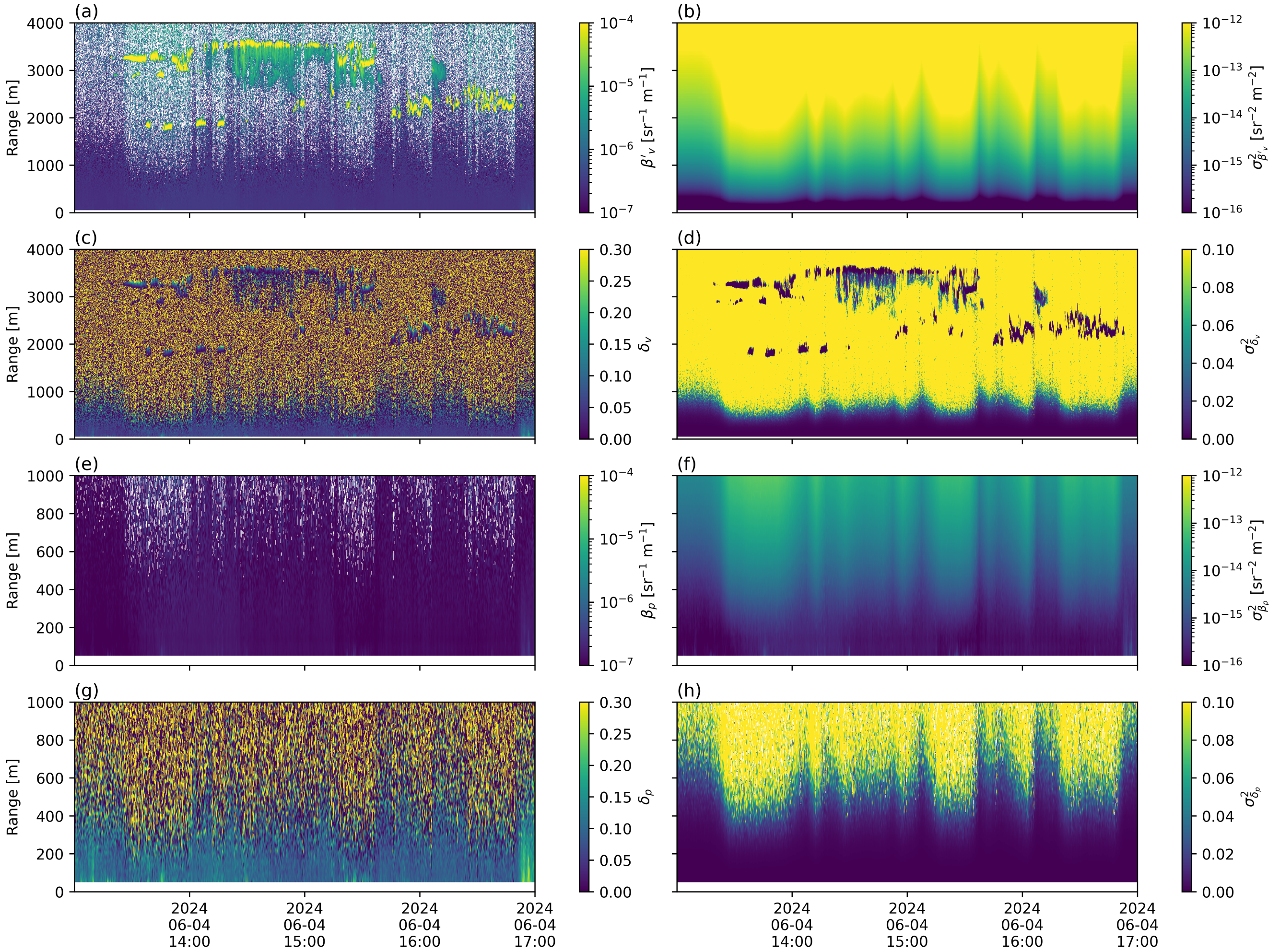

Figure 10. An example of corrected profile in Kenttärova on 2024-06-04 13:00 - 17:00 UTC (same day as Fig. 9). a) β'_v, b) $\sigma^2_{\beta_v}$ c) δ_v, d) $\sigma^2_{\delta_v}$ e) β_p, f) $\sigma^2_{\beta_p}$, g) δ_p, and h) $\sigma^2_{\delta_p}$.

https://doi.org/10.5194/egusphere-2025-6331
Preprint. Discussion started: 4 January 2026

4.5 Signal loss

As previously noted, abrupt changes in the cloud calibration factor at Vehmasmäki were observed from June to October 2023 and again from November to December 2024. Similar deviations are present during the same periods as seen in the window condition housekeeping variable (Fig. S9). These patterns indicate that an obstruction, likely on the instrument window, was attenuating both outgoing and incoming laser beams.

Figure 11 illustrates a specific example from 19 May, 2023. On this date, a sudden drop in the attenuated backscatter signal below $2000\ \mathrm{m}$ occurred just before 06:00 UTC. At the same time, the window condition value sharply declined from around 100% to 70%. This coincided with the automatic deactivation of the window blower heater. Housekeeping data, including internal temperature and relative humidity, were used to estimate the internal dew point, which was then compared to external air temperature. When the window blower heater was off, the window cooled to match the outside air temperature. Once the window temperature dropped below the internal dew point, condensation began to form on the surface and attenuated the signal.

Since condensation affects the entire signal profile and the degree of attenuation depends on its severity, it is not possible to precisely quantify the signal loss or reconstruct the original profile. To mitigate this issue, we recommend keeping both the window blower and heater on. Additionally, hardware modifications may be required to maintain a sufficiently low internal dew point and prevent fogging.

https://doi.org/10.5194/egusphere-2025-6331
Preprint. Discussion started: 4 January 2026

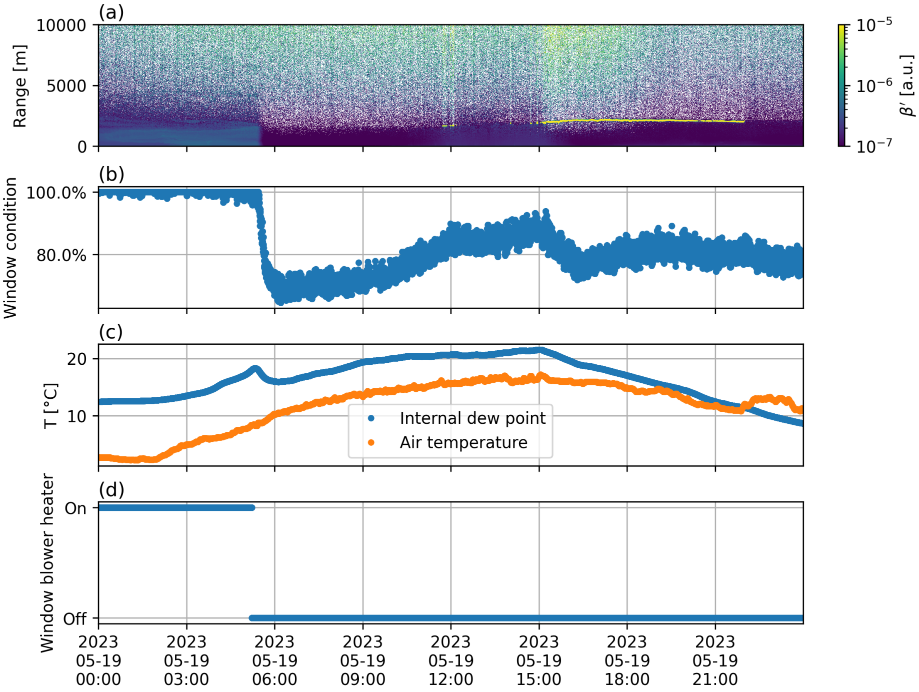

Figure 11. Measurements from Vehmasmäki on 2023-05-19 a) β', b) window condition, c) internal dew point and outside air temperature, c) window blower heater

5 Conclusions

In this study, we present a methodology for identifying the background signal and selecting suitable liquid cloud layers for quantifying temporal variations in background noise and determining the calibration factor over time. For most instruments, internal scaling of the calibration constant effectively compensates for changes in laser power. However, for the instrument at the Lindenberg site, this compensation becomes insufficient when laser power drops below 40%, resulting in a drift in the calibration factor. Therefore, regular cloud calibration is necessary to ensure quantitatively reliable profiles, especially when the laser power falls below 40%. Some deviations in the calibration factor were linked with internal fogging of the window.

Termination hood measurements were performed on selected instruments and proved effective in characterizing the instrument noise profile and the temperature dependence of the overlap function. Notably, differences in the instrumental bias were observed between parallel and perpendicular polarizations. The calibration profiles also reveal periodic variations in the near range signal below $50\ \mathrm{m}$ in both polarizations. As they appear sporadically, we recommend discarding the first $50\ \mathrm{m}$ of measurements. Instrumental bias profiles were obtained across a range of internal temperatures and were subsequently used to correct the bias and estimate its associated uncertainty. These profiles remained stable for at least one month for a given internal temperature, although small deviations appeared over a six-month period. Consequently, we recommend making termination-hood measurements every six months during continuous operation.

In a representative summer case study at Kenttärova, the instrumental bias corrected attenuated backscatter coefficient and depolarization ratio β_v and δ_v differ only slightly from their uncorrected counterparts β and δ, up to $2.5 \times 10^{-9}\ \mathrm{sr}^{-1}\ \mathrm{m}^{-1}$ and 0.005 respectively, reflecting the relatively small instrumental bias in both polarization channels compared with the atmospheric signal. Nevertheless, the termination hood measurements remain crucial, as they allow the instrumental noise to be quantified and thus enable the derivation of measurement uncertainties. The study also highlights the importance of accounting for the molecular contribution when quantitatively interpreting aerosol measurements with the CL61 ceilometer. We found that the difference between β_p and β is approximately $1.5 \times 10^{-7}\ \mathrm{sr}^{-1}\ \mathrm{m}^{-1}$, and that between δ and δ_p is roughly 0.1 in the near surface layer. These differences can be substantial when aerosol loading is low but they may also vary depending on the aerosol properties and prevailing atmospheric conditions.

Additionally, some instruments experienced signal loss caused by the fogging of the optical lens, which resulted in degraded data quality. Identifying and excluding such periods is essential for ensuring the integrity of the dataset and the reliability of subsequent analyses.

Data availability. The CL61 and model data used in this study are provided by the Aerosol, Clouds and Trace Gases Research Infrastructure (ACTRIS) and are available respectively from the ACTRIS Data Centre using the following DOIs: 10.60656/57adeb3f598243f2 and 10.60656/d2626d9dd3454006). The CL61 raw data was obtained from the landing page of the DOI.

Author contributions. VL, EOC and MF performed the terminal hood calibrations. VL prepared the manuscript. EOC, MF, VV contributed remarks and revisions on the manuscript.

Competing interests. The authors declare that they have no conflict of interest.

Acknowledgements. Financial support by Magnus Ehrnrooth Foundation is gratefully acknowledged. This project was supported by the 405 Research Council of Finland (grant no 337552, 343359). The authors also gratefully acknowledge the support of Vaikuttavuussäätiö (the Finnish Research Impact Foundation) through the Tandem Industry Academia (TIA) program. We also acknowledge ACTRIS, the Finnish Meteorological Institute, and the Lindenberg Meteorological Observatory - Richard Assmann Observatory (MOL-RAO) for providing the data set which is available for download from https://cloudnet.fmi.fi.

References

Baars, H., Kanitz, T., Engelmann, R., Althausen, D., Heese, B., Komppula, M., Preißler, J., Tesche, M., Ansmann, A., Wandinger, U., Lim, J. H., Young Ahn, J., Stachlewska, I. S., Amiridis, V., Marinou, E., Seifert, P., Hofer, J., Skupin, A., Schneider, F., Bohlmann, S., Foth, A., Bley, S., Pfüller, A., Giannakaki, E., Lihavainen, H., Viisanen, Y., Kumar Hooda, R., Pereira, S. N., Bortoli, D., Wagner, F., Mattis, I., Janicka, L., Markowicz, K. M., Achtert, P., Artaxo, P., Pauliquevis, T., Souza, R. A., Prakesh Sharma, V., Gideon Van Zyl, P., Paul Beukes, J., Sun, J., Rohwer, E. G., Deng, R., Mamouri, R. E., and Zamorano, F.: An overview of the first decade of PollyNET: An emerging network of automated Raman-polarization lidars for continuous aerosol profiling, Atmospheric Chemistry and Physics, 16, 5111–5137, https://doi.org/10.5194/acp-16-5111-2016, 2016.

Baars, H., Seifert, P., Engelmann, R., and Wandinger, U.: Target categorization of aerosol and clouds by continuous multiwavelength-polarization lidar measurements, Atmospheric Measurement Techniques, 10, 3175–3201, https://doi.org/10.5194/amt-10-3175-2017, 2017.

Barragán, R., Molero, F., Salvador, P., Theobald, M. R., Vivanco, M. G., Rodríguez-Sánchez, A., Gil, V., Garrido, J. L., Pujadas, M., and Artíñano, B.: Study of the Effect of Different Atmospheric Conditions on the Temporal Evolution of the Mixing Layer over Madrid during the Year 2020 by Means of Two Different Methods: Ceilometer Signals and the ECMWF-IFS Meteorological Model, Remote Sensing, 15, 5583, https://doi.org/10.3390/rs15235583, 2023.

Biele, J., Beyerle, G., and Baumgarten, G.: Polarization lidar: Corrections of instrumental effects, Optics Express, 7, 427–435, https://doi.org/10.1364/OE.7.000427, 2000.

Binietoglou, I., Amodeo, A., D'Amico, G., Giunta, A., Madonna, F., Mona, L., and Pappalardo, G.: Examination of possible synergy between lidar and ceilometer for the monitoring of atmospheric aerosols, in: Lidar Technologies, Techniques, and Measurements for Atmospheric Remote Sensing VII, vol. 8182, pp. 48–60, SPIE, https://doi.org/10.1117/12.897530, 2011.

Bucholtz, A.: Rayleigh-scattering calculations for the terrestrial atmosphere, Applied Optics, 34, 2765–2773, https://doi.org/10.1364/AO.34.002765, 1995.

Burton, S. P., Ferrare, R. A., Hostetler, C. A., Hair, J. W., Rogers, R. R., Obland, M. D., Butler, C. F., Cook, A. L., Harper, D. B., and Froyd, K. D.: Aerosol classification using airborne High Spectral Resolution Lidar measurements-methodology and examples, Atmospheric Measurement Techniques, 5, 73–98, https://doi.org/10.5194/amt-5-73-2012, 2012.

Campbell, J. R., Hlavka, D. L., Welton, E. J., Flynn, C. J., Turner, D. D., Spinhirne, J. D., Scott, V. S., and Hwang, I. H.: Full-Time, Eye-Safe Cloud and Aerosol Lidar Observation at Atmospheric Radiation Measurement Program Sites: Instruments and Data Processing, Journal of Atmospheric and Oceanic Technology, 19, 431–442, https://doi.org/10.1175/1520-0426(2002)019<0431:FTESCA>2.0.CO;2, 2002.

Cao, N., Zhu, C., Kai, Y., and Yan, P.: A method of background noise reduction in lidar data, Applied Physics B, 113, 115–123, https://doi.org/10.1007/s00340-013-5447-9, 2013.

Cimini, D., Haeffelin, M., Kotthaus, S., Löhnert, U., Martinet, P., O'Connor, E., Walden, C., Coen, M. C., and Preissler, J.: Towards the profiling of the atmospheric boundary layer at European scale—introducing the COST Action PROBE, Bulletin of Atmospheric Science and Technology, 1, 23–42, https://doi.org/10.1007/s42865-020-00003-8, 2020.

Donovan, D. P., Klein Baltink, H., Henzing, J. S., De Roode, S. R., and Siebesma, A. P.: A depolarisation lidar-based method for the determination of liquid-cloud microphysical properties, Atmospheric Measurement Techniques, 8, 237–266, https://doi.org/10.5194/amt-8-237-2015, 2015.

Fernald, F. G., Herman, B. M., and Reagan, J. A.: Determination of Aerosol Height Distributions by Lidar, Journal of Applied Meteorology and Climatology, 11, 482–489, https://doi.org/10.1175/1520-0450(1972)011<0482:DOAHDB>2.0.CO;2, 1972.

Filioglou, M., Leskinen, A., Vakkari, V., O'Connor, E., Tuononen, M., Tuominen, P., Laukkanen, S., Toiviainen, L., Saarto, A., Shang, X., Tiitta, P., and Komppula, M.: Spectral dependence of birch and pine pollen optical properties using a synergy of lidar instruments, Atmospheric Chemistry and Physics, 23, 9009–9021, https://doi.org/10.5194/acp-23-9009-2023, 2023.

Filioglou, M., Tiitta, P., Shang, X., Leskinen, A., Ahola, P., Pätsi, S., Saarto, A., Vakkari, V., Isopahkala, U., and Komppula, M.: Lidar estimates of birch pollen number, mass, and CCN-related concentrations, Atmospheric Chemistry and Physics, 25, 1639–1657, https://doi.org/10.5194/acp-25-1639-2025, 2025.

Floutsi, A. A., Baars, H., Engelmann, R., Althausen, D., Ansmann, A., Bohlmann, S., Heese, B., Hofer, J., Kanitz, T., Haarig, M., Ohneiser, K., Radenz, M., Seifert, P., Skupin, A., Yin, Z., Abdullaev, S. F., Komppula, M., Filioglou, M., Giannakaki, E., Stachlewska, I. S., Janicka, L., Bortoli, D., Marinou, E., Amiridis, V., Gialitaki, A., Mamouri, R.-E., Barja, B., and Wandinger, U.: DeLiAn – a growing collection of depolarization ratio, lidar ratio and Ångström exponent for different aerosol types and mixtures from ground-based lidar observations, Atmospheric Measurement Techniques, 16, 2353–2379, https://doi.org/10.5194/amt-16-2353-2023, 2023.

Freudenthaler, V., Esselborn, M., Wiegner, M., Heese, B., Tesche, M., Ansmann, A., Müller, D., Althausen, D., Wirth, M., Fix, A., Ehret, G., Knippertz, P., Toledano, C., Gasteiger, J., Garhammer, M., and Seefeldner, M.: Depolarization ratio profiling at several wavelengths in pure Saharan dust during SAMUM 2006, Tellus B, 61, 165–179, https://doi.org/10.1111/j.1600-0889.2008.00396.x, 2009.

Görsdorf, U., Komppula, M., Moisseev, D., and O'Connor, E.: Custom collection of lidar data from Hyytiälä, Kenttärova, Lindenberg, and Vehmasmäki between 1 Oct 2021 and 31 Dec 2024, https://doi.org/10.60656/D2626D9DD3454006, 2025.

Haeffelin, M., Laffineur, Q., Bravo-Aranda, J.-A., Drouin, M.-A., Casquero-Vera, J.-A., Dupont, J.-C., and De Backer, H.: Radiation fog formation alerts using attenuated backscatter power from automatic lidars and ceilometers, Atmospheric Measurement Techniques, 9, 5347–5365, https://doi.org/10.5194/amt-9-5347-2016, 2016.

Hervo, M., Poltera, Y., and Haefele, A.: An empirical method to correct for temperature-dependent variations in the overlap function of CHM15k ceilometers, Atmospheric Measurement Techniques, 9, 2947–2959, https://doi.org/10.5194/amt-9-2947-2016, 2016.

Hirsikko, A., O'Connor, E. J., Komppula, M., Korhonen, K., Pfüller, A., Giannakaki, E., Wood, C. R., Bauer-Pfundstein, M., Poikonen, A., Karppinen, T., Lonka, H., Kurri, M., Heinonen, J., Moisseev, D., Asmi, E., Aaltonen, V., Nordbo, A., Rodriguez, E., Lihavainen, H., Laaksonen, A., Lehtinen, K. E. J., Laurila, T., Petäjä, T., Kulmala, M., and Viisanen, Y.: Observing wind, aerosol particles, cloud and precipitation: Finland's new ground-based remote-sensing network, Atmospheric Measurement Techniques, 7, 1351–1375, https://doi.org/10.5194/amt-7-1351-2014, 2014.

Hopkin, E., Illingworth, A. J., Charlton-Perez, C., Westbrook, C. D., and Ballard, S.: A robust automated technique for operational calibration of ceilometers using the integrated backscatter from totally attenuating liquid clouds, Atmospheric Measurement Techniques, 12, 4131–4147, https://doi.org/10.5194/amt-12-4131-2019, 2019.

Hämäläinen, K., Hirsikko, A., Leskinen, A., Komppula, M., O'Connor, E. J., and Niemelä, S.: Evaluating atmospheric icing forecasts with ground-based ceilometer profiles, Meteorological Applications, 27, e1964, https://doi.org/10.1002/met.1964, 2020.

Illingworth, A. J., Barker, H. W., Beljaars, A., Ceccaldi, M., Chepfer, H., Clerbaux, N., Cole, J., Delanoë, J., Domenech, C., Donovan, D. P., Fukuda, S., Hirakata, M., Hogan, R. J., Huenerbein, A., Kollias, P., Kubota, T., Nakajima, T., Nakajima, T. Y., Nishizawa, T., Ohno, Y., Okamoto, H., Oki, R., Sato, K., Satoh, M., Shephard, M. W., Velázquez-Blázquez, A., Wandinger, U., Wehr, T., and Van Zadelhoff, G. J.: The earthcare satellite : The next step forward in global measurements of clouds, aerosols, precipitation, and radiation, Bulletin of the American Meteorological Society, 96, 1311—1332, https://doi.org/10.1175/BAMS-D-12-00227.1, 2015.

Illingworth, A. J., Cimini, D., Haefele, A., Haeffelin, M., Hervo, M., Kotthaus, S., Löhnert, U., Martinet, P., Mattis, I., O'Connor, E. J., and Potthast, R.: How Can Existing Ground-Based Profiling Instruments Improve European Weather Forecasts?, Bulletin of the American Meteorological Society, 100, 605–619, https://doi.org/10.1175/BAMS-D-17-0231.1, 2019.

Klett, J. D.: Lidar inversion with variable backscatter/extinction ratios, Applied Optics, 24, 1638–1643, https://doi.org/10.1364/AO.24.001638, 1985.

Kotthaus, S., O'Connor, E., Münkel, C., Charlton-Perez, C., Haeffelin, M., Gabey, A. M., and Grimmond, C. S. B.: Recommendations for processing atmospheric attenuated backscatter profiles from Vaisala CL31 ceilometers, Atmospheric Measurement Techniques, 9, 3769–3791, https://doi.org/10.5194/amt-9-3769-2016, 2016.

Kotthaus, S., Bravo-Aranda, J. A., Collaud Coen, M., Guerrero-Rascado, J. L., Costa, M. J., Cimini, D., O'Connor, E. J., Hervo, M., Alados-Arboledas, L., Jiménez-Portaz, M., Mona, L., Ruffieux, D., Illingworth, A., and Haeffelin, M.: Atmospheric boundary layer height from ground-based remote sensing: a review of capabilities and limitations, Atmospheric Measurement Techniques, 16, 433–479, https://doi.org/10.5194/amt-16-433-2023, 2023.

Le, V., Lobo, H., O'Connor, E. J., and Vakkari, V.: Long-term aerosol particle depolarization ratio measurements with HALO Photonics Doppler lidar, Atmospheric Measurement Techniques, 17, 921–941, https://doi.org/10.5194/amt-17-921-2024, 2024.

Lee, G., Gommers, R., Waselewski, F., Wohlfahrt, K., and O'Leary, A.: PyWavelets: A Python package for wavelet analysis, Journal of Open Source Software, 4, 1237, https://doi.org/10.21105/joss.01237, 2019.

Mamouri, R. E. and Ansmann, A.: Potential of polarization lidar to provide profiles of CCN-and INP-relevant aerosol parameters, Atmospheric Chemistry and Physics, 16, 5905–5931, https://doi.org/10.5194/acp-16-5905-2016, 2016.

Martucci, G., Milroy, C., and O'Dowd, C. D.: Detection of Cloud-Base Height Using Jenoptik CHM15K and Vaisala CL31 Ceilometers, Journal of Atmospheric and Oceanic Technology, 27, 305–318, https://doi.org/10.1175/2009JTECHA1326.1, 2010.

Nason, G. P. and Silverman, B. W.: The Stationary Wavelet Transform and some Statistical Applications, pp. 281–299, Springer New York, New York, NY, https://doi.org/10.1007/978-1-4612-2544-7_17, 1995.

Nicolae, D., Vasilescu, J., Talianu, C., Binietoglou, I., Nicolae, V., Andrei, S., and Antonescu, B.: A neural network aerosol-typing algorithm based on lidar data, Atmospheric Chemistry and Physics, 18, 14 511–14 537, https://doi.org/10.5194/acp-18-14511-2018, 2018.

O'Connor, E.: Model data from Kenttärova on 5 March 2024, https://hdl.handle.net/21.12132/1.b218f85f5ed14149, 2024.

O'Connor, E.: Custom collection of model data from Hyytiälä, Kenttärova, Lindenberg, and Vehmasmäki between 1 Oct 2021 and 31 Dec 2024, https://doi.org/10.60656/57ADEB3F598243F2, 2025.

O'Connor, E. J., Illingworth, A. J., and Hogan, R. J.: A technique for autocalibration of cloud lidar, Journal of Atmospheric and Oceanic Technology, 21, 777–786, https://doi.org/10.1175/1520-0426(2004)021<0777:ATFAOC>2.0.CO;2, 2004.

Ribaud, J.-F., Haeffelin, M., Dupont, J.-C., Drouin, M.-A., Toledo, F., and Kotthaus, S.: PARAFOG v2.0: a near-real-time decision tool to support nowcasting fog formation events at local scales, Atmospheric Measurement Techniques, 14, 7893–7907, https://doi.org/10.5194/amt-14-7893-2021, 2021.

Rocadenbosch, F., Barragán, R., Frasier, S. J., Waldinger, J., Turner, D. D., Tanamachi, R. L., and Dawson, D. T.: Ceilometer-Based Rain-Rate Estimation: A Case-Study Comparison With S-Band Radar and Disdrometer Retrievals in the Context of VORTEX-SE, IEEE Transactions on Geoscience and Remote Sensing, 58, 8268–8284, https://doi.org/10.1109/TGRS.2020.2984458, 2020.

Roschke, J., Witthuhn, J., Klingebiel, M., Haarig, M., Foth, A., Kötsche, A., and Kalesse-Los, H.: Discriminating between "drizzle or rain" and sea salt aerosols in Cloudnet for measurements over the Barbados Cloud Observatory, Atmospheric Measurement Techniques, 18, 487–508, https://doi.org/10.5194/amt-18-487-2025, 2025.

Sassen, K.: The Polarization Lidar Technique for Cloud Research: A Review and Current Assessment, Bulletin of the American Meteorological Society, 72, 1848–1866, https://doi.org/10.1175/1520-0477(1991)072<1848:TPLTFC>2.0.CO;2, 1991.

Shang, X., Mielonen, T., Lipponen, A., Giannakaki, E., Leskinen, A., Buchard, V., Darmenov, A. S., Kukkurainen, A., Arola, A., O'Connor, E., Hirsikko, A., and Komppula, M.: Mass concentration estimates of long-range-transported Canadian biomass burning aerosols from a multi-wavelength Raman polarization lidar and a ceilometer in Finland, Atmospheric Measurement Techniques, 14, 6159–6179, https://doi.org/10.5194/amt-14-6159-2021, 2021.

Tomasi, C., Vitale, V., Petkov, B., Lupi, A., and Cacciari, A.: Improved algorithm for calculations of Rayleigh-scattering optical depth in standard atmospheres, Applied Optics, 44, 3320–3341, https://doi.org/10.1364/AO.44.003320, 2005.

Tsaknakis, G., Papayannis, A., Kokkalis, P., Amiridis, V., Kambezidis, H. D., Mamouri, R. E., Georgoussis, G., and Avdikos, G.: Intercomparison of lidar and ceilometer retrievals for aerosol and Planetary Boundary Layer profiling over Athens, Greece, Atmospheric Measurement Techniques, 4, 1261–1273, https://doi.org/10.5194/amt-4-1261-2011, 2011.

Uzan, L., Egert, S., Khain, P., Levi, Y., Vadislavsky, E., and Alpert, P.: Ceilometers as planetary boundary layer height detectors and a corrective tool for COSMO and IFS models, Atmospheric Chemistry and Physics, 20, 12 177–12 192, https://doi.org/10.5194/acp-20-12177-2020, 2020.

Van der Kamp, D.: Ceilometer observations of Vancouver's urban boundary layer : validation and mixed-layer height estimation, Ph.D. thesis, University of British Columbia, https://doi.org/10.14288/1.0066572, 2008.

Wandinger, U.: Introduction to Lidar, in: Lidar: Range-Resolved Optical Remote Sensing of the Atmosphere, edited by Weitkamp, C., pp. 1–18, Springer New York, New York, NY, https://doi.org/10.1007/0-387-25101-4_1, 2005.

Warren, E., Charlton-Perez, C., Kotthaus, S., Lean, H., Ballard, S., Hopkin, E., and Grimmond, S.: Evaluation of forward-modelled attenuated backscatter using an urban ceilometer network in London under clear-sky conditions, Atmospheric Environment, 191, 532–547, https://doi.org/10.1016/j.atmosenv.2018.04.045, 2018.

Welton, E. J. and Campbell, J. R.: Micropulse Lidar Signals: Uncertainty Analysis, Journal of Atmospheric and Oceanic Technology, 19, 2089–2094, https://doi.org/10.1175/1520-0426(2002)019<2089:MLSUA>2.0.CO;2, 2002.

Wiegner, M. and Geiß, A.: Aerosol profiling with the Jenoptik ceilometer CHM15kx, Atmospheric Measurement Techniques, 5, 1953–1964, https://doi.org/10.5194/amt-5-1953-2012, 2012.

Wiegner, M., Madonna, F., Binietoglou, I., Forkel, R., Gasteiger, J., Geiß, A., Pappalardo, G., Schäfer, K., and Thomas, W.: What is the benefit of ceilometers for aerosol remote sensing? An answer from EARLINET, Atmospheric Measurement Techniques, 7, 1979–1997, https://doi.org/10.5194/amt-7-1979-2014, 2014.